ADVANCING EARTH AND SPACE SCIENCES

JGR Solid Earth

RESEARCH ARTICLE
10.1029/2024JB030633

Co-Evolution of Specific Stiffness and Permeability of Rock Fractures Offset in Shear

Xinxin He[1], Pengliang Yu[1,2], Agathe Eijsink[1,2], Chris Marone[1,3], Parisa Shokouhi[4], Jacques Rivière[4], Shimin Liu[1], and Derek Elsworth[1,2]

[1]Energy and Mineral Engineering, Pennsylvania State University, University Park, PA, USA, [2]Department of Geosciences, Pennsylvania State University, University Park, PA, USA, [3]Dipartimento di Scienze della Terra, La Sapienza Università di Roma, Rome, Italy, [4]Engineering Science and Mechanics, Pennsylvania State University, University Park, PA, USA

Key Points:

- Numerical simulations on granular mechanics models define the relationship between specific stiffness and permeability in rough fractures under stress
- Increased surface roughness and larger shear offsets result in microcracking, reduced stiffness and reduced sensitivity of permeability to stress
- Stiffness is linearly related to normalized geometry (offset, wavelength, and elastic modulus) and permeability, presenting stiffness as diagnostic for shear-offset fractures

Supporting Information:

Supporting Information may be found in the online version of this article.

Correspondence to:

X. He and D. Elsworth,
xinxinheest@gmail.com;
elsworth@psu.edu

Citation:

He, X., Yu, P., Eijsink, A., Marone, C., Shokouhi, P., Rivière, J., et al. (2025). Co-evolution of specific stiffness and permeability of rock fractures offset in shear. *Journal of Geophysical Research: Solid Earth*, *130*, e2024JB030633. https://doi.org/10.1029/2024JB030633

Received 31 OCT 2024
Accepted 4 MAY 2025

Author Contributions:

Conceptualization: Xinxin He, Derek Elsworth
Formal analysis: Xinxin He
Funding acquisition: Derek Elsworth
Investigation: Xinxin He, Derek Elsworth
Methodology: Xinxin He, Derek Elsworth
Project administration: Derek Elsworth
Resources: Chris Marone, Parisa Shokouhi, Jacques Rivière, Shimin Liu, Derek Elsworth
Software: Xinxin He
Supervision: Shimin Liu, Derek Elsworth

Abstract Fractures and faults represent planes of weakness and compliance in rock masses that serve as focal points for both microearthquakes and fluid transport, with seismicity and permeability evolution closely linked. Contact stiffness is highly stress-sensitive and directly influences permeability. We explore the co-evolution of specific stiffness and permeability of rough fractures under normal stress and shear offset using numerical simulations. Individual rough fractures are represented by variable amplitude (Root mean square) and wavelength (λ) using a granular mechanics model. Contacting rough surfaces are mated, offset in shear, and then compacted in displacement mode. The compacting fractures generate stress-dependent changes in contact porosity, which govern both permeability and stiffness evolution. We establish a universal dimensionless relationship linking specific stiffness and permeability that inherently incorporates the effects of surface roughness, shear offset, and microcracking. The observed cracking effect—where local stress redistribution and pressure-driven microcrack propagation dynamically alter the aperture field—introduces a nonlinear permeability response at high stress. Increased roughness amplitude and larger shear offsets reduce stiffness while dampening permeability sensitivity to stress, demonstrating a strong interplay between surface texture and hydro-mechanical behavior. While the model captures this behavior effectively, deviations emerge at very low porosities due to extreme aperture sensitivity in this limit.

Plain Language Summary Fractures and faults in rocks act as pathways for fluids and sites for earthquakes. Both fluid flow and how easily fractures deform depend on the size and distribution of voids—suggesting that knowledge of one provides insight into the other. Since fracture stiffness can be measured using seismic waves, this implies that remote sensing techniques could also be used to infer fluid flow characteristics (permeability). In our study, we used numerical simulations to explore how fractures with different surface roughness and sliding movements (offsets) change under stress. As the fractures are compressed, their void structure evolves, influencing both their ability to transmit fluids and their mechanical response. We identify a universal dimensionless relationship linking fracture stiffness and permeability, which accounts for roughness, offset, and microcracking. Additionally, we observe a cracking effect, where local stress changes lead to microcrack growth, unexpectedly altering permeability in certain regions. Our findings provide a framework for predicting fracture behavior, with potential applications in geophysics, hydrocarbon extraction, and engineered fluid transport systems.

1. Introduction

Carbon capture and storage, hydrocarbon storage and extraction, enhanced shale gas and coalbed methane recovery (ECBM) and enhanced geothermal systems all require the injection and/or extraction of fluids into/from the crust. Elevated pore pressures change effective stresses and may reactivate faults (Elsworth et al., 2016; Guglielmi et al., 2015) and generate permeability that may allow fugitive emission of the injected fluids. Understanding such changes is important in characterizing the performance of such activities in the deep subsurface.

Discontinuum models of rock masses (Cook, 1992; Goodman, 1975; Goodman et al., 1968; Leopold Müller, 1963; Talobre, 1957) offer critical insights into how fractured rock formations deform and conduct fluids under varying stresses and pressures. As fractures and faults substantially affect both stiffness and flow paths, they must be explicitly accounted for in any realistic geomechanical assessment. Characteristics of stiffness and permeability may be defined by the structure of individual fractures—specifically by geometrical parameters of aperture distribution and asperity height defining void space and connectivity and controlling permeability

Validation: Xinxin He, Chris Marone, Parisa Shokouhi, Jacques Rivière, Derek Elsworth
Visualization: Xinxin He
Writing – original draft: Xinxin He
Writing – review & editing: Pengliang Yu, Agathe Eijsink, Chris Marone, Parisa Shokouhi, Jacques Rivière, Shimin Liu, Derek Elsworth

(Brown et al., 1998; Méheust & Schmittbuhl, 2000). Since contact morphology and void connectivity and topology are sensitive to stress, permeability is also stress sensitive. In addition, fracture contact stiffness changes with applied stress rendering fracture stiffness and permeability potentially linked. The geometry of fractures controls both the hydraulic and mechanical properties of rock, two crucial aspects in subsurface response—with the relationship and interplay between these properties of profound importance. Hydraulic studies have focused on evaluating the effects of laminar and mixed laminar/turbulent flow in rock fissures (Elsworth, 1984), examining the validity of the cubic law for deformable rock fractures (Witherspoon et al., 1980), defining the flow-deformation response of fissured media (Elsworth & Mao, 1992) and in introducing models that incorporate fracture permeability and the serial processes of dissolution at contacting asperities (Yasuhara et al., 2004). Field observations confirm that transient stresses alter permeability (Manga et al., 2012) and resulting adjusted flow regimes impact the stability and integrity of rock structures and fluid production and injection characteristics. Fracture closure and hence permeability change is controlled by specific stiffness - defined as the reciprocal of fracture closure with incremented normal stress. Relations between geometric and mechanical properties (Bandis et al., 1983; Goodman, 1975; Goodman et al., 1968; Swan, 1983; Zimmerman & Bodvarsson, 1996) ultimately link these to diagnostic measurements that probe fracture stiffness, as fracture stiffness strongly impacts hydromechanical behavior. Ultrasonic methods, initially applied in the early 1990s (Myer et al., 1990; Pyrak-Nolte & Nolte, 1992; Pyrak-Nolte et al., 1990a, 1990b), have further evolved to incorporate cross-coupling modes during shearing (Choi et al., 2014; Nakagawa et al., 2003, 2004); and to encompass both laboratory (Lubbe et al., 2008; Shokouhi et al., 2020; Wood et al., 2024) and field-scale applications (Worthington, 2007, 2008). In parallel, geophysical techniques such as electrical resistivity (Charles, 2018; Sawayama et al., 2023) and heat transfer measurements (Luo et al., 2016; Martínez et al., 2014) have also proven valuable for understanding how fractures control fluid flow and rock mass response.

Both qualitative and quantitative relationships are available, linking permeability and specific stiffness through fracture geometry. Some models incorporate statistical distributions of roughness and aperture (Petrovitch et al., 2014; Pyrak-Nolte, 2019; Pyrak-Nolte & Nolte, 2016; L. Wang & Cardenas, 2016) linked to elastic-wave and electrical resistivity to link fracture stiffness to permeability (Pyrak-Nolte & Morris, 2000; Sawayama et al., 2023). Indeed, rough fractures may be characterized (Petrovitch et al., 2014; Pyrak-Nolte, 2019; Pyrak-Nolte & Nolte, 2016), but often employ simplified representations, such as cylindrical rods termed "bed-of-nails" (Gangi, 1978), sinusoidal models (Elsworth, 1984), or elliptical-asperity models (Greenwood, 1967). Bed-of-nails (or similar) approaches typically treat asperities as discrete rods deforming under Hertzian contact with other models incorporating asperity interactions and matrix deformation (Hopkins, 1991). This model has been further developed and studied extensively (Pyrak-Nolte, 2019; Pyrak-Nolte & Morris, 2000; Pyrak-Nolte & Nolte, 2016; L. Wang & Cardenas, 2016). Loss of detail in such models may be incorporated as natural rough surfaces (Bowden & Tabor, 1950; McCool, 1986; Whitehouse & Archard, 1970) (Figure S1a in Supporting Information S1) that accommodate plastic response at microcontacts before becoming elastically stable (Archard, 1957; Bowden & Tabor, 1950). Finally, many previous models, including those performing well in linear elastic response (Hopkins, 1991; Petrovitch et al., 2014; Pyrak-Nolte & Nolte, 2016), significantly advanced our understanding of the normal deformation of fracture surfaces. However, these frameworks inherently focus on reversible elastic behavior, leaving irreversible processes (e.g., bond breakage) and 3D asperity failure mechanisms observed in natural fractures undefined. To address these limitations, Discrete Element Methods (DEM) have been used to represent irregular fracture surfaces and their non-linear responses under load. These include investigations into strength and permeability evolution during compaction (Zheng & Elsworth, 2012, 2013), fracture propagation with elevated pore pressure (K. Wang et al., 2022; Yang et al., 2020) and stability analyses of excavations in hard rock (Hadjigeorgiou et al., 2009) as well as responses to varying loading rates and fracture dip angles (T. Wang et al., 2023; Zhao et al., 2015). However, the majority of DEM studies remain confined to 2D.

We address these limitations by exploring the specific stiffness to permeability response of 3D rough and statistically equivalent contacting fracture surfaces of defined macroscale roughness under shear offset. These granular mechanics models incorporate local failure at fine-scale and resulting production of comminution/wear products that impact the evolution of both specific stiffness and related permeability. These models define a full spectrum of shear offsets to one full long-wavelength roughness and for varying contact roughness amplitudes. Granular mechanics models allow for a more flexible representation of the microscale response of fracture by detailing the stochastic nature of contact force orientations (Figure S1b in Supporting Information S1). This feature makes them useful for studying nonlinear contact evolution under shear offset, where contact geometry and force distributions change dynamically.

2. Numerical Simulation Approach

We explore the stress-stiffness-permeability relationship, that is, the co-evolution of specific stiffness and permeability under stress and shear offset, in rough fractures using a granular mechanics model. Specifically, we explore the role of fracture roughness and shear offset to represent shear reactivation of idealized faults. Rough fractures are offset in shear to represent conditions of misalignment and then define stiffness and corresponding evolution in permeability. We construct rough fractures to a defined morphology using a granular mechanics model and mechanically compress the virtual model. We jointly recover the evolution of stiffness and permeability and link these two parameters. The entire process is reflected in Figure 1 flowchart.

2.1. Fracture Surface Generation

We characterize fracture roughness in terms of a statistical representation of a surface represented by sinusoidal asperity height and wavelength, overprinted by random noise. Peak heights of surface asperities follow a Gaussian distribution typically used to simulate rock joint properties (Swan, 1983) with randomly distributed noise. The two controlling parameters are: (a) Root mean square (RMS) height, S_q, of the asperities, and (b) Correlation wavelength, λ, defining the length over which variables are correlated. The RMS of the asperities on a surface of area A is:

$$S_q = \sqrt{\frac{1}{A}\iint z^2(x,y)\,dx\,dy} \tag{1}$$

where $z\ (x,\ y)$ represents the elevation of an individual asperity relative to its spatial location.

On an isotropic surface, the Gaussian filter function F is defined as:

$$F(x,y) = e^{\left(\frac{x^2+y^2}{\lambda^2}\right)} \tag{2}$$

to give the final surface elevation $Z\ (x,\ y)$ by applying this Gaussian filter F to the initial Gaussian surface $z\ (x,\ y)$ through Fourier transformation and then taking the inverse Fourier transform:

$$Z(x,y) = \frac{2}{\sqrt{\pi}}\sqrt{\frac{A}{N_x \cdot N_y}}\ \frac{1}{\lambda} \tag{3}$$

where N_x and N_y are the number of sampled increments along traverses in the x- and y-directions, respectively. Notably, Equation 3 represents a reduced form expression (see Equation S1 in Supporting Information S1 for the complete formulation).

We simultaneously vary RMS amplitude S_q and correlation wavelength λ in the two orthogonal directions (x- and y-direction) in the plane of the fracture by isotropically applying Gaussian filtering within the average plane of the fracture as shown in Figure 1a. This approach allows us to effectively characterize and straightforwardly quantify different roughness profiles.

Additionally, while S_q generally increases the roughness profiles of fractures, λ smooths the profile and reduces roughness. Recent investigations (Candela et al., 2012) highlight that the S_q is largely independent of short-range correlation lengths. We therefore define a non-dimensional roughness-to-wavelength ratio, α, as **:**

$$\alpha = \frac{S_q}{\lambda} \tag{4}$$

to quantify these effects and represent the roughness, where increasing roughness-to-wavelength ratio, α, indicates a progressively rougher surface.

10.1029/2024JB030633

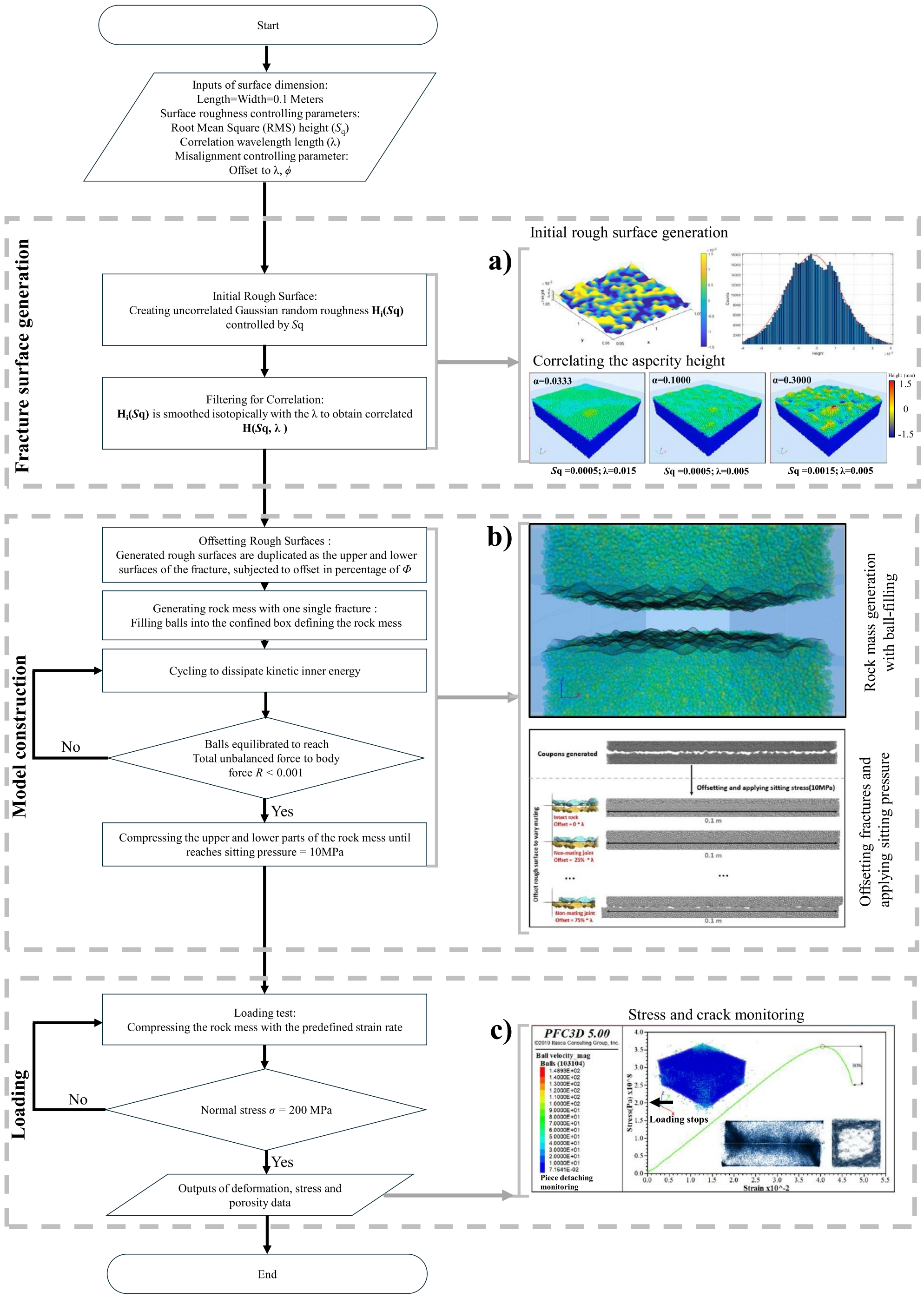

Figure 1. Flowchart showing the workflow in defining the mechanical response of a single rough rock fracture using granular mechanics simulations.

2.2. DEM Model Construction

We use the Particle Flow Code (PFC^{3D}) as a suitable granular mechanics model accommodating rigid spherical particles (Cundall & Strack, 1979). We generate fracture surfaces with predefined roughness using a sinusoidal fracture with overprinted Gaussian noise (Figure 1a). These digital rock surfaces are utilized to simulate the dynamic response of fractures under normal loading. Although generalizable in terms of geometry and dimension, the analyses are conducted on a fracture plane 0.1 × 0.1 m on edge and ~0.01 m in height, with superposed

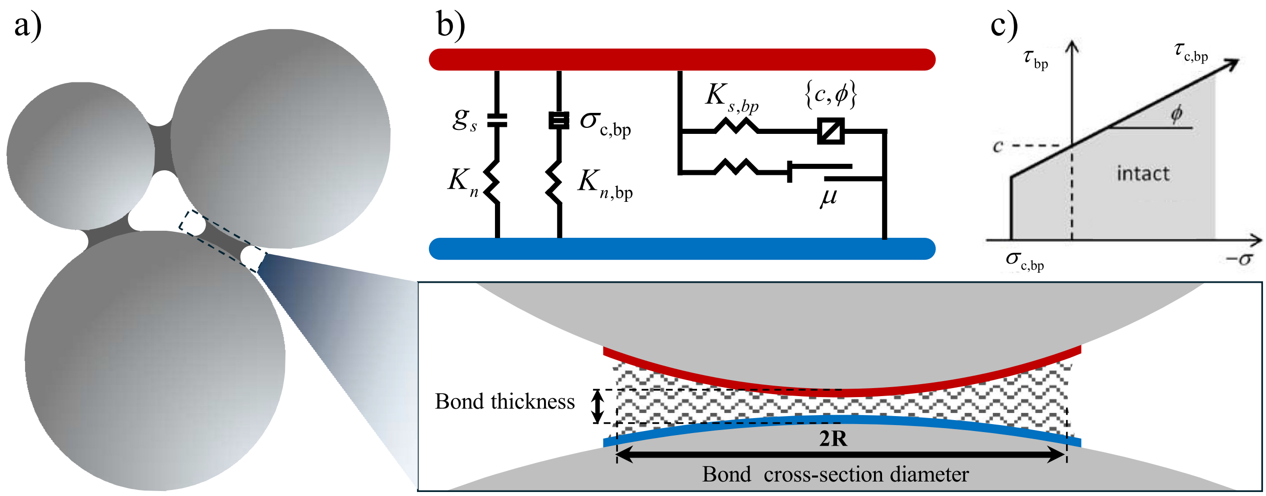

Figure 2. (a) Contact model and rheological components of the linear parallel bond model with inactive dashpots; (b) Failure envelope for the parallel bond.

roughness. The fractures are formed by filling a virtual container with spherical particles, where one side is formed by the rough contact surface (Figure 1b). Two such rough-surfaced fracture halves are placed face-to-face, consolidated to dissipate unbalanced forces through the damping factor, then are bonded to form cohesive and lithified samples using a contact model, described in detail later in Section 2.3. Subsequently, the contacting fracture halves, each with corresponding mated fracture surfaces, are carefully aligned, brought together, then further loaded. This replicates the initial conditions of the contacting surfaces prior to the application of normal stress. Thus, it is important to clarify that the specific stiffness examined in this study specifically refers to normal specific stiffness, in contrast to shear stiffness, which has been explored in prior studies (Choi et al., 2014). In separate simulations, the aligned upper and lower contacting rough fractures are separately shear-offset by quarter-fractions of 0.25, 0.5 and 0.75 of the correlation wavelength in the x-direction (lower Figure 1b), to simulate mismatch. A seating stress of 10 MPa is applied before further closure is driven in displacement mode at a predefined strain rate of $10^{-6}\ s^{-1}$ to 200 MPa to avoid edge effects (Petrovitch et al., 2014). A damping factor of 0.7 is used throughout the experiment to control the dissipation of kinetic energy in the numerical model, ensuring numerical stability and preventing excessive oscillations in the system.

2.3. Contact Model

In granular mechanics models in general, and PFC^{3D} in particular, particles interact through internal forces at their contact points. The models employ a soft-contact approach, where deformation is confined to the points of contact between rigid bodies (Cundall & Strack, 1979). These interactions are regulated by specific particle-interaction laws, known as contact models. Each point of contact is governed by an individual contact model, ensuring precise control over the mechanical interactions. We use a linear parallel bond (LPB) model (Figure 2a) to describe the interaction. The first component is an infinitesimal, linear elastic (no-tension) and frictional interface that transmits a force. The second component is a finite-size, linear elastic and bonded interface that transmits both a force and a moment (Figure 2b). As the key control in this model, a brief introduction of the LPB is given here. The force within an LPB contact is:

$$F_c = F_l + F_{pb} + F_d \tag{5}$$

where F_l is the linear force, F_{pb} is the parallel-bond force and F_d is the viscous dashpot force for energy dissipation. The linear force response is fundamental in contact mechanics and is primarily governed by normal stiffness (K_n), shear stiffness (K_s), and the friction coefficient (μ), which serve as the first order parameters excercizing (Figure 2b) contact control in the model (Potyondy & Cundall, 2004). These parameters define the linear contact interactions and influence the mechanical behavior of the fracture system. The force in the parallel bond is separated into normal and shear components, while the moment in the parallel bond is divided into twisting and bending moments as:

$$F_{\mathrm{pb}} = -F_{\mathrm{pb}}^{n} n_{\mathrm{c}} + F_{\mathrm{pb}}^{s} \tag{6}$$

$$M_{\mathrm{pb}} = M_{\mathrm{pb}}^{\mathrm{t}} n_{\mathrm{c}} + M_{\mathrm{pb}}^{\mathrm{b}} \tag{7}$$

where F_{pb}^{n} and F_{pb}^{s} are the normal and shear components of the parallel-bond force F_{pb}; F_{pb}^{t} and F_{pb}^{b} are the twisting and bending components of the parallel-bond moment M_{pb} and $\boldsymbol{n}_c$ is the unit normal vector of the contact surface. Those components are evaluated from their dependent constituents in each step of the simulation, and are updated as:

$$F_{\mathrm{pb}}^{\mathrm{n}} = F_{\mathrm{pb}}^{\mathrm{n}} + K_{n,\mathrm{bp}} A_c \Delta\delta_n \tag{8}$$

$$F_{\mathrm{pb}}^{s} = F_{\mathrm{pb}}^{s} - K_{s,\mathrm{bp}} A_{\mathrm{c}} \Delta\delta_s \tag{9}$$

$$M_{\mathrm{pb}}^{\mathrm{t}} = K_{s,\mathrm{bp}} J\theta_{\mathrm{t}} \tag{10}$$

$$M_{\mathrm{pb}}^{\mathrm{b}} = K_{n,\mathrm{bp}} I\theta_{\mathrm{b}} \tag{11}$$

where A_c is the contact cross-sectional area; $\Delta\delta_n$ and $\Delta\delta_s$ are the incremental normal and shear displacements within the contact; I is the moment of inertia of the cross-section; J is the polar moment of inertia of the cross-section; and θ_t and θ_b are the twisting and bending angles of the contact, respectively. Thus, the tensile and shear stresses within the parallel bond are defined as:

$$\sigma_{\mathrm{bp}} = \frac{F_{\mathrm{bp}}^{n}}{A_c} + \beta_{\mathrm{bp}} \frac{\left\| M_{\mathrm{bp}}^{\mathrm{b}} \right\| R}{I} \tag{12}$$

$$\tau_{\mathrm{bp}} = \frac{F_{\mathrm{bp}}^{s}}{A_c} + \beta_{\mathrm{bp}} \frac{\| M_{\mathrm{bp}}^{\mathrm{t}} \| R}{J} \tag{13}$$

where β_{bp} is the moment-contribution factor in the range [0,1] and R is the contact cross-section radius. In each contact computation cycle, the parallel bond acts to resist relative rotation and maintains linear elastic behavior until the strength limit is reached and the bond breaks ($\sigma_{\mathrm{bp}} > \sigma_{\mathrm{c,bp}}$ and $\tau_{\mathrm{bp}} > \tau_{\mathrm{c,bp}}$ as shown in Figure 2c the LPB failure envelope), debonding the particles. Once debonded, the linear contact stiffness and rolling resistance carry the following updates of the contact force and follow shear slip evolution based on K_{n}, K_{s}, and μ. Table 2 summarizes the key model parameters adopted in this study, chosen to reflect the properties of a stiff sandstone.

3. Results

We explore the effects of surface roughness and shear displacement offset under applied normal stress on the co-evolution of fracture permeability and specific stiffness. We link stiffness to changes in fracture permeability by placing fiducial measurement spheres across the fracture to track changes in porosity. Fracture closure is analyzed in relation to pre-defined surface roughness and shear offset to codify the co-evolution of specific stiffness and permeability.

3.1. Porosity Evolution With Shear Offset

A total of 17 fiducial measurement spheres are positioned centrally across the fracture to track the evolution of local porosity during loading. As shown in Figure 3, the measurement spheres are identically located for all shear offset experiments. Measurement windows are divided into two groups: central spheres (highlighted with blue dots) which assess the local porosity at the center of the virtual sample, and peripheral spheres (highlighted with red dots), which monitor the conditions at the sample edge.

Evolving porosity profiles for a mid-roughness fracture ($\alpha = 0.1000$; $S_{\mathrm{q}} = 0.0005$, $\lambda = 0.005$) are shown in Figure 4. For zero offset ($\phi = 0.00$) the average local porosity adjacent to the fracture is consistent with that of the bulk (defined in Table 2) but rises with increasing misalignment. Thus, the fully aligned sample ($\phi = 0.00$) serves

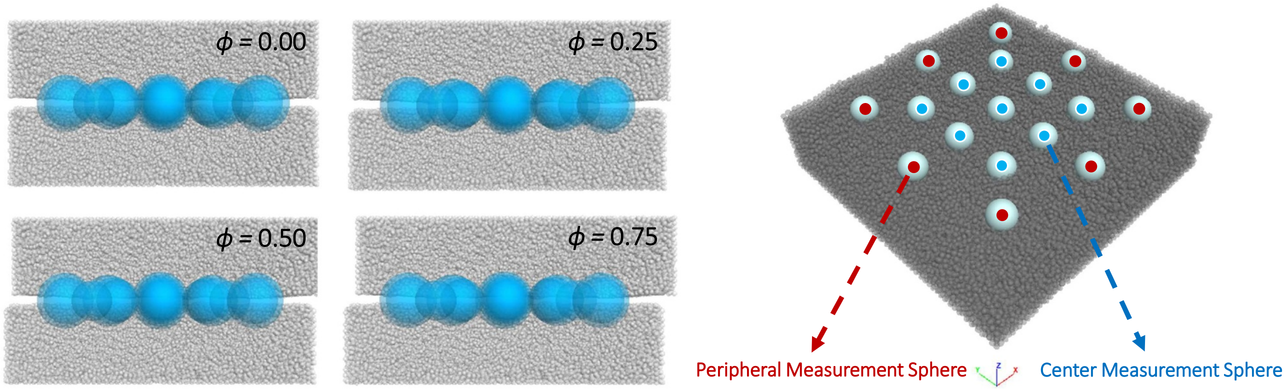

Figure 3. Location of the measurement balls/spheres.

as the baseline for calculating shear displacement induced joint closure, defined as the axial displacement difference between mismatched and fully aligned configurations. Most bond-breakages occur for a three-quarter-wavelength shear offset ($\phi = 0.75$). The bond-breakages (red symbols in the base of Figure 4) are more widespread at higher offsets but remain concentrated around major asperities (Figure 5). As offset increases, the stress threshold for crack initiation decreases, due to elevated contact stresses. A sublinear increase in crack number with respect to ϕ is observed, highlighting the relationship between geometric alignment and material response under stress. This understanding is essential for predicting material behavior in geological formations and other applications. Although small differences are observed in porosity between the center and edges for each shear offset, we see no significant clustering of cracks (Figure 5) or uneven contact area distribution (Figure S4). This finding suggests that, up to 200 MPa, edge effects remain comparatively negligible in our simulations.

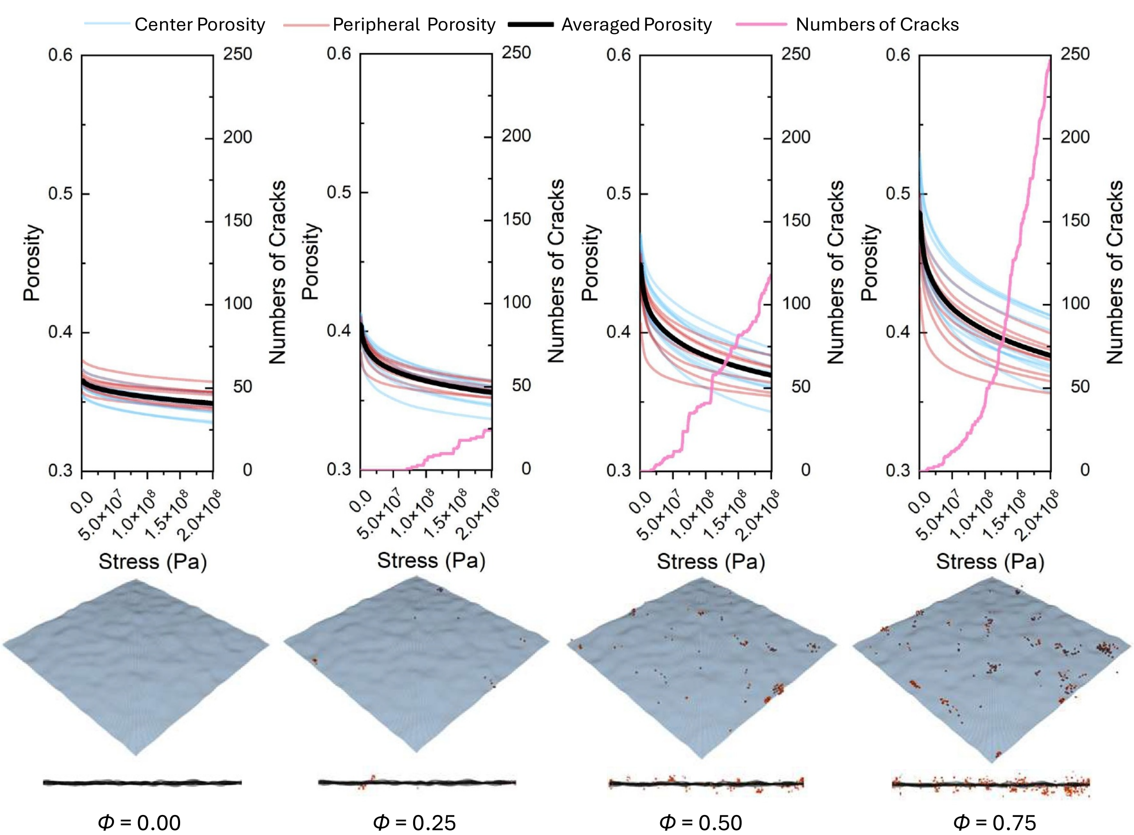

Figure 4. Porosity profile of the rock fracture with $\alpha = 0.1000$.

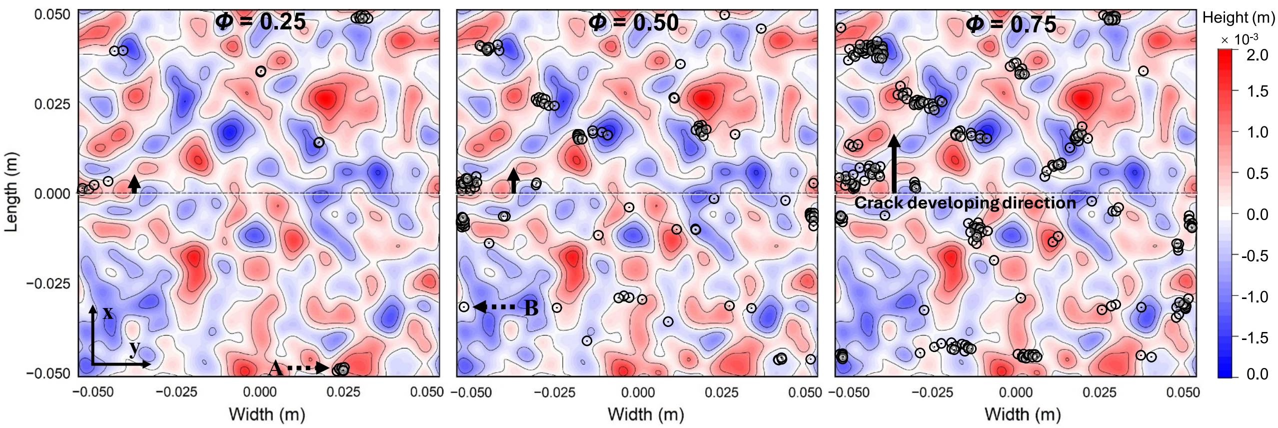

Figure 5. Correlation between crack locations and fracture topography with $\alpha = 0.1000$.

To establish the correlation between crack locations and surface topography, Figure 5 displays an elevation map of the fracture surface, with crack positions marked by black circles. The spatial analysis reveals that cracks, perhaps surprisingly, systematically avoid topographic peaks and troughs, instead forming within transitional zones between these features. This spatial relationship suggests that crack initiation is governed by interfacial shear stresses generated through misalignment of the upper and lower surfaces. Specifically, the initial contact areas between opposing asperities experience concentrated shear stresses, particularly on the edge of the shear offset direction where initial contact area is larger than the other edge. As the offset ϕ increases, crack evolution exhibits two characteristic behaviors: progressive development of new cracks along the shear direction in regions sustaining persistent contact, and elimination of pre-existing cracks in areas losing mechanical contact due to asperity separation. For instance, crack A observed at $\phi = 0.25$ disappears at $\phi = 0.50$ as its host asperities disengage, while crack B at $\phi = 0.50$ vanishes upon reaching $\phi = 0.75$.

3.2. Fracture Closure With Stress

An increase in normal stress results in increasing joint closure (Figure 6). Rougher fractures are progressively less stiff, as are fractures with increasing shear offset (Figure 6) (Bandis et al., 1983). Thus, as both surface roughness and fracture offset increase, joint closure becomes more pronounced. Interestingly, this joint closure is highly comparable to the change observed in the aperture distribution (Figure S2 in Supporting Information S1). Notably, under elevated stresses, there is a linear region, particularly evident in samples with smoother and well-mated surfaces. The variations in joint closure for different offsets becomes increasingly marked—with a fivefold increase in closure for the smoothest to roughest fracture for a shear offset of $\phi = 0.75$. Additionally, the breakage of bonds contributes to increased development of rupture (cracking) with sudden jumps in the closure apparent.

3.3. Evolution of Specific Stiffness

Specific stiffness is calculated from its definition (Bandis et al., 1983) (Table 1):

$$Kn = \frac{\Delta\sigma}{\Delta d} \tag{14}$$

where $\Delta\sigma$ is the change in applied normal stress and Δd is the change in fracture closure.

Stiffness decreases as surface roughness increases, indicating a mechanistic correlation between roughness and mechanical stiffness (Figure 7). Additionally, greater shear mismatch between contacting surfaces reduces stiffness, especially for smoother fractures. Noise within the displacement response (Figure 7) reflects individual bond breakage events and the potential creation of wear products. These dynamics, which may not be captured by traditional linear models, highlight the value of using the DEM approach in following a more realistic material contact response (Potyondy & Cundall, 2004; Wang et al., 2020; Zheng & Elsworth, 2013).

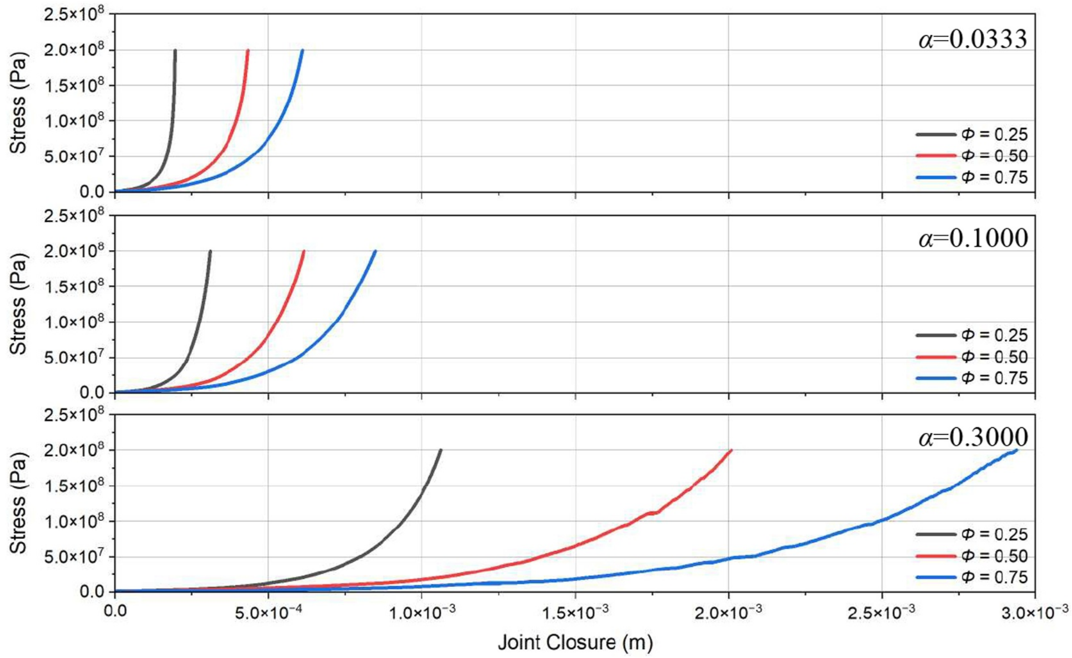

Figure 6. Joint closure under normal stress up to 200 MPa for different surface roughness.

3.4. Evolution of Fracture Permeability

Based on the aperture distribution profile obtained from the DEM model (by taking the difference in asperity height between the upper and lower fracture surfaces as shown in Figure S3), we conducted flow simulations using the parallel plate approximation corresponding to incremented normal stresses where specific stiffnesses are also known. Incremented stresses ranged from an initial 1 MPa (the same as the initial seating stress of the

Table 1
Geometric Parameters and Related Mechanical and Hydraulic Properties

Parameters	Definitions	Illustration
Aperture	$b = h_{\text{fractured}} - h_{\text{intact}}$	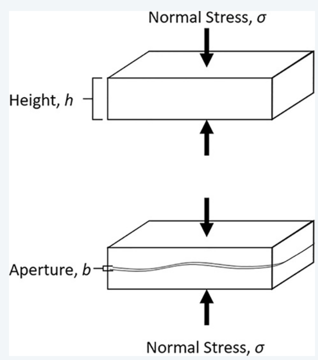
Axial displacement	$\delta = h_0 - h$	
Joint closure	$d = \delta_{\text{fractured}} - \delta_{\text{intact}}$	
Specific stiffness	$Kn = \frac{\Delta\sigma}{\Delta d}$	
Permeability change	$\frac{k}{k_0} = \left(1 + \frac{b - b_0}{b_0}\right)^3$	

Joint closure d as a function of h	Aperture b as a function of h	Relationship between b, d.
$d = \delta_{\text{fractured}} - \delta_{\text{intact}}$	$b - b_0 = (h_{\text{fractured}} - h_{\text{intact}}) - (h_{\text{fractured}} - h_{\text{intact}})_0$	$b - b_0 = -d$
$d = (h_o - h)_{\text{fractured}} - (h_o - h)_{\text{intact}}$	$b - b_0 = h_{\text{fractured}} - h_{\text{intact}} - h_{0,\text{ fractured}} + h_{0,\text{intact}}$	
$d = h_{0,\text{fractured}} - h_{\text{fractured}} - h_{0,\text{intact}} + h_{\text{intact}}$	$b - b_0 = -\left(-h_{\text{fractured}} + h_{\text{intact}} + h_{0,\text{ fractured}} - h_{0,\text{intact}}\right)$	

Note. Subscript: fractured (attributes of the fractured rock), intact (attributes of the intact rock), 0 (before loading).

Table 2
Model Parameter Inputs

Parameters	Values	Reference
Sample porosity	0.3600	(Dyke & Dobereiner, 1991; Gottsmann et al., 2019)
Damping factor	0.7000	–
Contacted fracture length and width, m.	0.1000	–
Minimum particle diameter, m.	0.0008	–
Maximum particle diameter, m.	0.0010	–
Particle density, kg/m^3	2,691.00	(Dyke & Dobereiner, 1991)
Bulk effective modulus, LK_n, Pa.	4.0×10^{10}	(Y. Wang et al., 2020; Yin et al., 2017)
Shear to Normal stiffness ratio K_s/K_n.	1.0000	(Cundall & Strack, 1979; Potyondy & Cundall, 2004)
Bond effective modulus, 2R$K_{n,bp}$, Pa.	1.0×10^9	(Cundall & Strack, 1979; Potyondy & Cundall, 2004)
Parallel bond shear to normal stiffness ratio, $K_{s,bp}/K_{n,bp}$.	1.0000	(Cundall & Strack, 1979; Potyondy & Cundall, 2004)
Particle inter-friction, μ.	0.5700	(Byerlee, 1978; Yoon, 2007)
Parallel bond tensile strength $\tau_{c,bp}$, Pa.	1.0×10^8	(Antony et al., 2018; Yoon, 2007)
Parallel bond cohesion, c, Pa.	1.0×10^9	(Cundall & Strack, 1979; Potyondy & Cundall, 2004)

DEM simulation) then in 20 steps from 10 to 200 MPa at equal increments of 10 MPa, to evaluate the evolution of permeability. The simulations employed a finite difference method, with fluid flowing horizontally, along the shear direction, across the fracture domain between opposing constant pressure boundaries of 20 kPa upstream (Figure 8, left) to 0 kPa downstream (right), and no-flow boundaries at the top and bottom. Detailed methodology can be found in Im et al. (2019).

Flow rate decreases significantly at the initial stage but stabilizes during later loading, as shown in Figure 8. Additionally, increasing the offset enhances the flow rate by generating larger apertures and more efficient flow channels. Interestingly, the closure of old flow pathways and the formation of new ones occur simultaneously during the loading process. For instance, when comparing the flow patterns at $\phi = 0.25$ between $\sigma = 150$ and

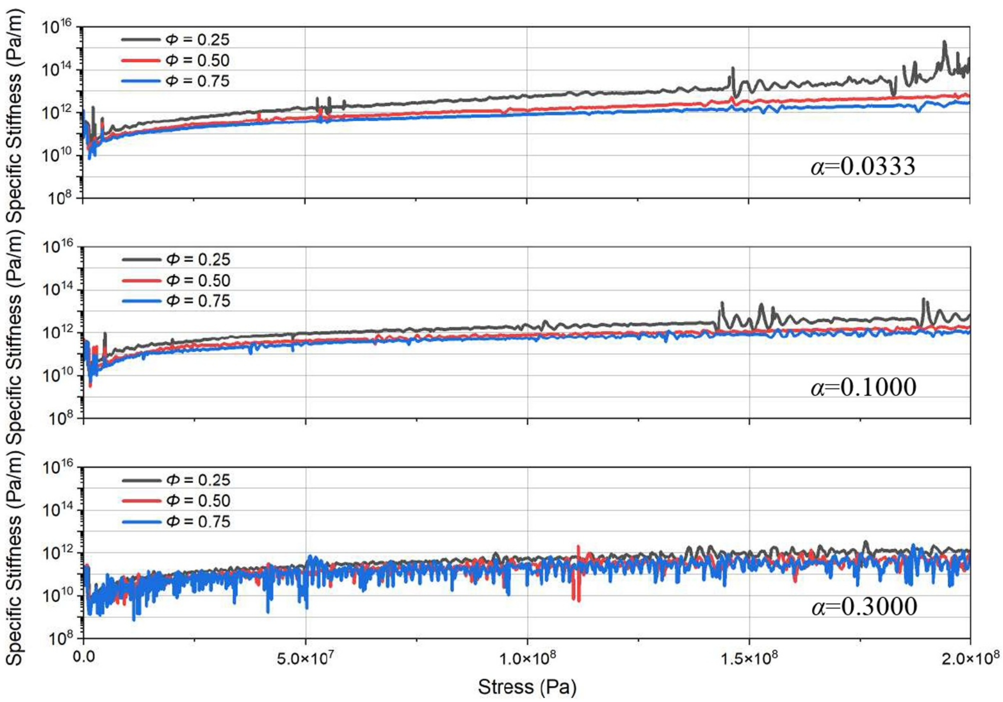

Figure 7. Relationship between specific stiffness and its corresponding applied stress.

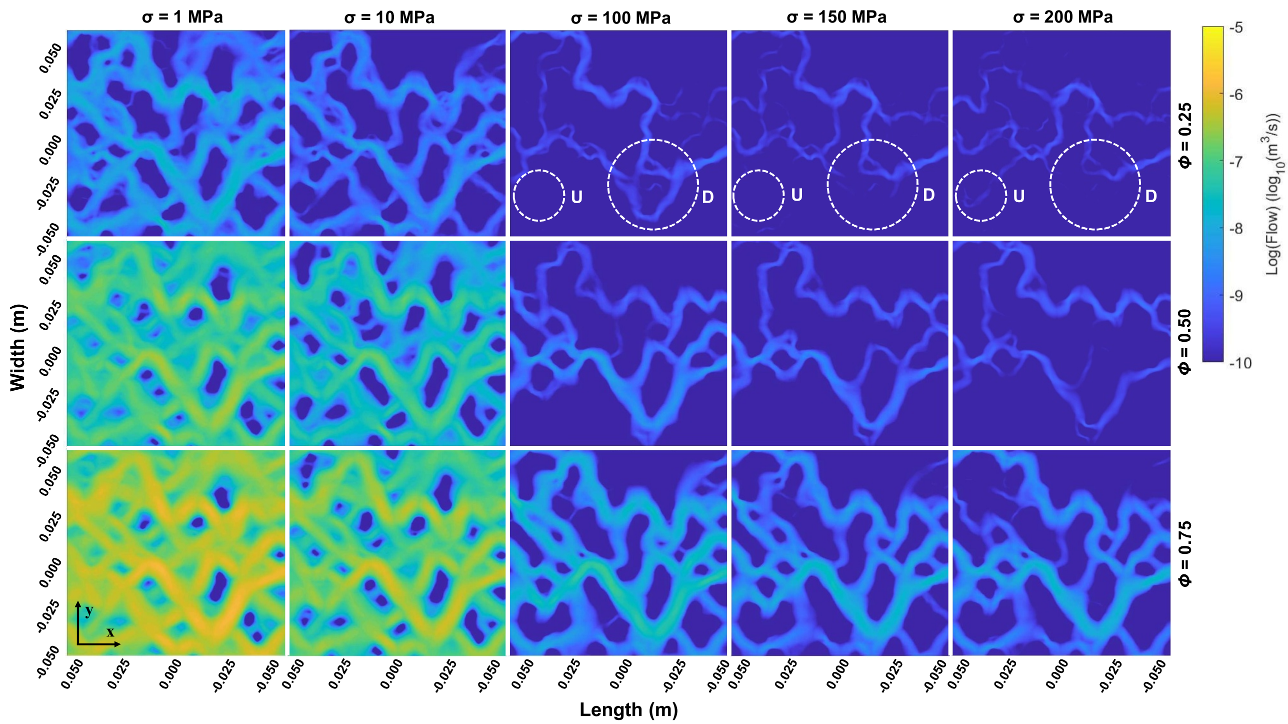

Figure 8. Fracture flow rate evolution under changing stress for fracture with $\alpha = 0.1000$.

200 MPa, the total flow rate continues to decline despite the reorganization of the flow in these channels, that is, the downstream region (D) ceases to conduct flow, whereas upstream flow (U) is reactivated. Pressure distributions along the newly reactivated flow path (Figure 9a to 9b) show a distinct pressure drop at 200 MPa, implying that local pressure gradients drive flow redistribution. Additionally, cracks (Figure 9, black circles) tend to cluster near the ends of this flow path, suggesting that fracture propagation or microcracking can locally alter the aperture distribution. Beyond ~100 MPa, the aperture distribution (Figure S4 in Supporting Information S1) appears relatively stable, but certain regions, particularly those along the reactivated flow path, exhibit localized aperture reversal (Figure S4d in Supporting Information S1): instead of continuing to reduce with rising stress, aperture can expand if cracking or local stress perturbations allow fluid to pry open small areas. At higher stress

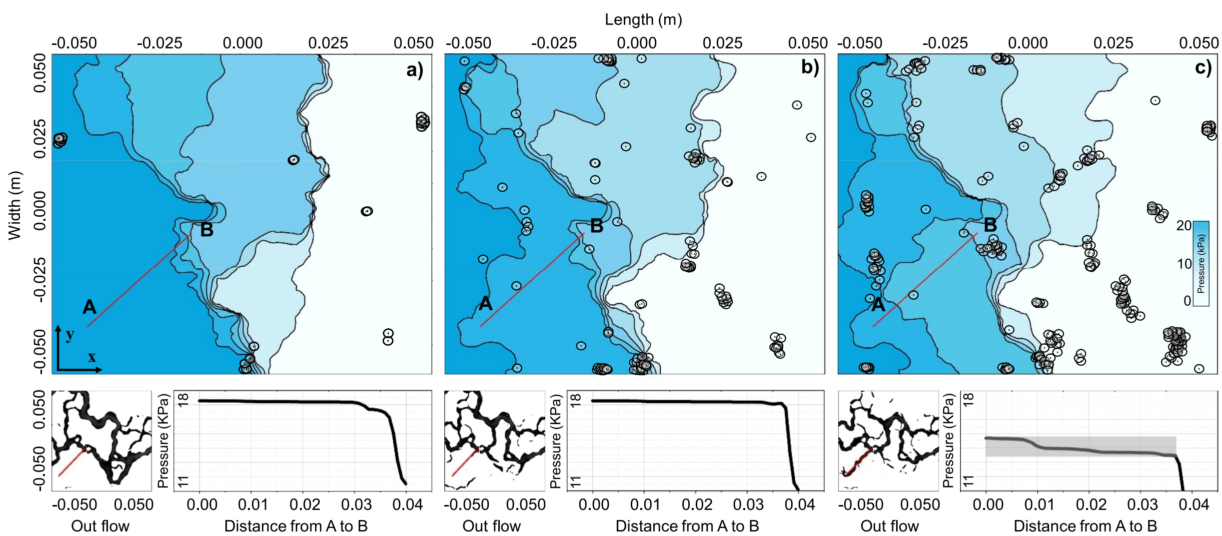

Figure 9. Fluid pressure profile for fracture with $\alpha = 0.1000$, $\phi = 0.25$: (a) $\sigma = 100$ MPa; (b) $\sigma = 150$ MPa; (c) $\sigma = 200$ MPa.

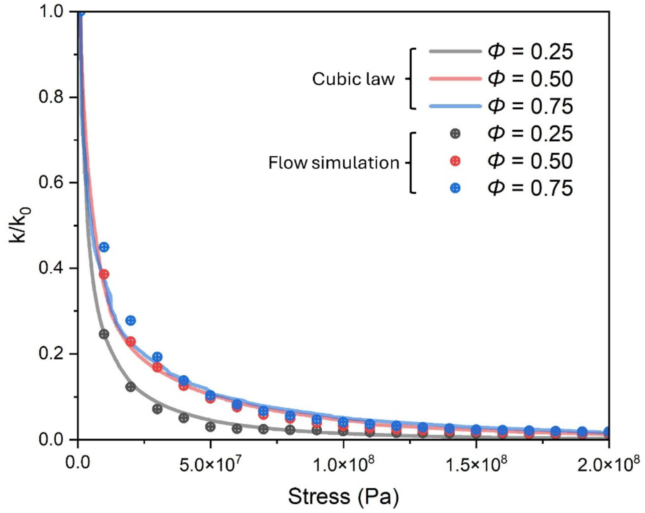

Figure 10. Effective permeability evolution with stress from both flow simulations (symbols) and assuming a uniform aperture as Equation 16.

levels, some previously contacting regions (Figure S4 in Supporting Information S1, near A) lose contact, indicating localized shifts in contact area due to particle displacement.

This "cracking effect" indicates that fracture reorganization arises from an interplay of fluid pressure, critical neck constriction, and microstructural damage. Mechanically, increasing stress narrows or closes critical necks once a threshold is reached, leading to reduced or ceased flow in certain areas. These blockages increase flow resistance, which in turn elevates local pressure gradients. If microcracks occur or existing cracks coalesce, the aperture in these zones can partially reopen, rediverting flow. Consequently, necks that closed at lower stress might reopen under higher stress if the local pressure gradient surpasses the reopening threshold. This cyclical opening/closing emphasizes the dynamic nature of flow channels under evolving stress and highlights how localized cracking can override the expected monotonic decrease in fracture aperture. This observed cracking effect underscores the complex interplay between stress, aperture evolution, and flow redistribution. Further investigations incorporating variations in bond strength could provide deeper insights into its influence on fracture permeability and the dynamic instability of flow pathways under evolving stress conditions.

Effective permeability k/k_0 evolution is evaluated from the flow simulations using Darcy's law:

$$Q = \frac{kA}{\mu L}\Delta p \tag{15}$$

where Q is the flow rate (m^3/s), k is the permeability (m^2) and A is the cross-sectional area of the fracture (m^2). In the case of 2D flow, A corresponds to the product of aperture b and flow width W, both in meters (m). μ is the dynamic viscosity of water (Pa.s), L is the length of sample (m) and Δp is the pressure drop (Pa).

The effective permeability evolution exhibited sharp declines at the onset of loading, aligning with the initial drop in flow rate as apparent in Figure 8. Changes in permeability with stress (Figure 10) are determined from the displacement closure response—that elicits a specific closure magnitude for each stress. Permeability reduces most rapidly with increasing stress for smaller shear offsets—representing better-matched fracture surfaces. Additionally, the effective permeability evolution profile is co-plotted and compared (Figure 10) using the evolution of an assumed uniform average aperture distribution from the DEM model and applying the cubic law (Wang et al., 2020; Zimmerman & Yeo, 2000):

$$\frac{k}{k_0} = \left(1 + \frac{b - b_0}{b_0}\right)^3 \tag{16}$$

where b is the aperture and b_0 is the initial aperture before loading, both in meters (m).

Except for an initial deviation at $\phi = 0.75$, the results from the flow simulation and the assumed uniform aperture are highly consistent (Figure 10). This confirms that the simplified approximation using the standard cubic law, which relies on an average fracture aperture derived from joint closure data, effectively captures the dominant trends in permeability evolution while avoiding the complexity of fully resolving localized flow paths (Wang et al., 2020; Witherspoon et al., 1980). Moreover, the simplification of Equation 16 facilitates continuous analysis, replacing the discrete results of the flow simulation. Thus, a continuous evolution of permeability with normal stresses was then evaluated, as presented in Figure 11. The results indicate that rougher fractures maintain higher effective permeabilities under the same normal stress. This suggests that smoother fractures, though potentially stiffer, undergo more significant permeability changes under stress.

We use stress as a common index to reference both specific stiffness (Figure 7) and permeability (Figure 11) and thus link permeability to specific stiffness (Figure 12). Specific stiffness is most sensitive to initial loading with all

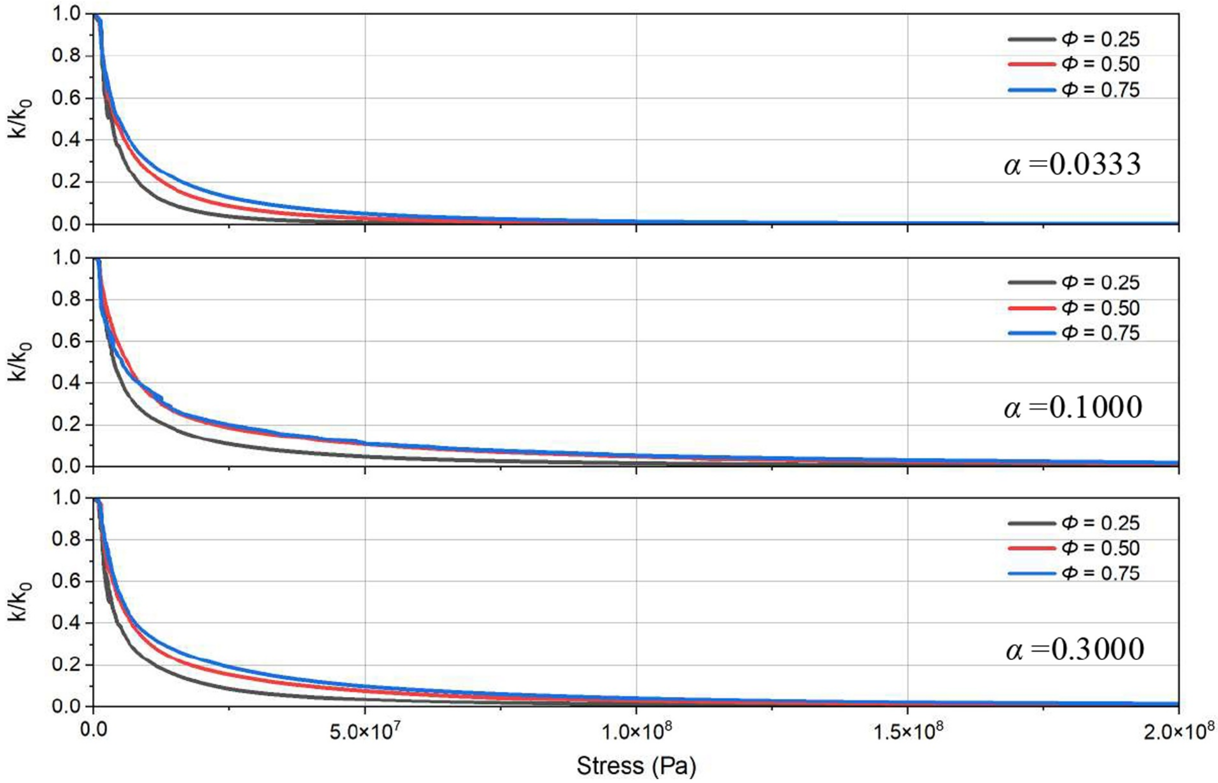

Figure 11. Permeability evolution under applied normal stress on different rough surfaces.

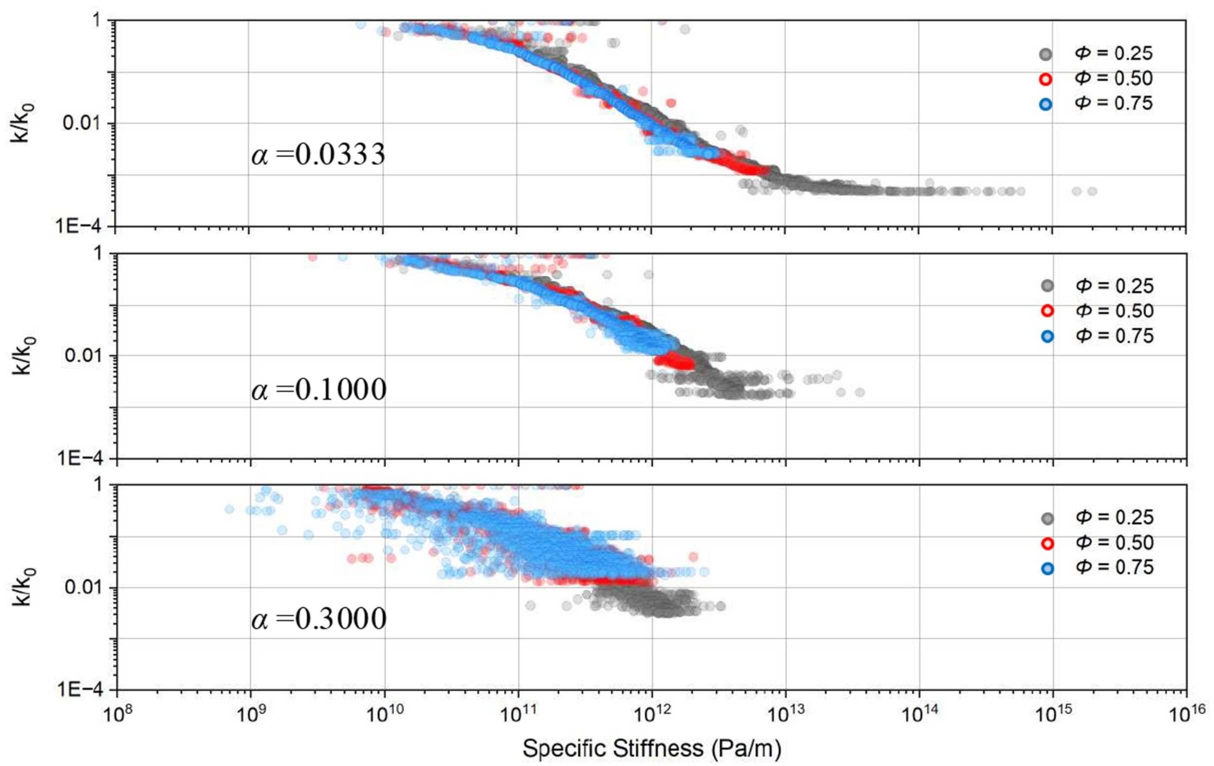

Figure 12. Relationship between specific stiffness and permeability.

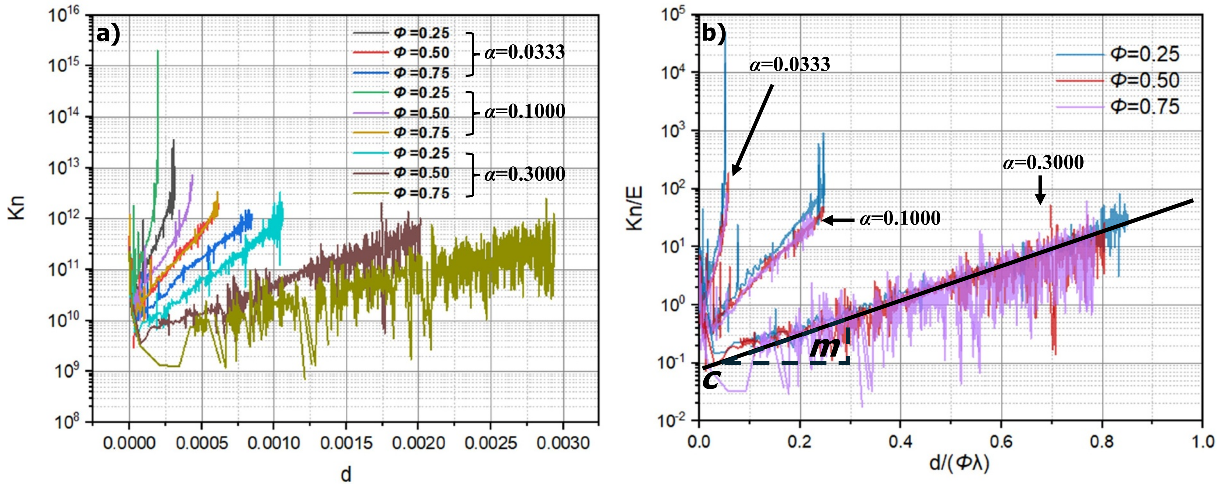

Figure 13. Relationship between the specific stiffness and (a) Dimensional and then (b) Normalized fracture closure.

permeabilities declining from an initial plateau in the log-log plot, suggesting changes in permeability primarily occur only when fractures stiffen considerably. This effect is more pronounced for smoother fractures ($\alpha = 0.0333$), where a broader and more distinct plateau is evident. From this plateau, permeabilities decrease with increasing stiffness—representing the stiffening with the reduction in porosity. These findings are consistent with prior studies (Petrovitch et al., 2013, 2014; Pyrak-Nolte, 2019; Pyrak-Nolte & Nolte, 2016) indicating two regimes for flow-stiffness behavior: an "effective medium" regime where permeability depends on initial rapid fracture porosity decrease (Figure 4), and a "percolation" regime in which flow requires interconnected channels (Figure 8), that is, In Figure 11, the observed initial plateau, reflecting the effective medium domain, followed by a rapid decline in permeability once critical apertures constrict sufficiently to disrupt flow paths. This hints to the potential for a dimensionless relationship that governs this interaction between these two parameters (permeability-stiffness) under stress (Cook, 1992; Petrovitch et al., 2013, 2014; Pyrak-Nolte, 2019; Pyrak-Nolte & Nolte, 2016). However, this decrease in permeability with increasing stiffness ceases as local porosity stabilizes at residual values (Figure 5), particularly evident for smooth fractures where permeability asymptotes to a constant. This response may represent the inability of the permeability model to correctly compute permeabilities at low porosities where the porosity is no longer connected and Equation 16 will overestimate permeability, where more complex conditions — for example, higher stresses approaching bulk failure, frictional gouge generation, or mixed-mode fracturing. In real experiments, such factors often lead to earlier and more pronounced deviations from closure-based permeability estimates.

4. Discussion

We explore the relationship between specific stiffness and fracture geometry to develop a predictive dimensionless relationship linking specific stiffness and permeability that incorporates surface roughness and shear offset.

4.1. Linear Relationship Between Specific Stiffness and Normalized Geometry

We explore the response of specific stiffness to fracture geometric parameters to 200 MPa. A strong linear relationship between the logarithm of specific stiffness and joint closure is apparent (Figure 13a), albeit with noticeable dispersion. This is especially apparent as joint closure increases and seems random across conditions.

We normalize geometric parameters and mechanical properties. Fracture closure is normalized by shear offset and correlation wavelength as $d/(\phi\lambda)$ and specific stiffness is normalized by elastic modulus as *Kn/E*. The normalized curves for a single fracture converge and overlap independent of different shear offsets (Figure 13b), in contrast to the separations for the dimensional curves (Figure 13a). This is mathematically represented by the relationship (Figure 13b):

10.1029/2024JB030633

$$\log(Kn/\mathrm{E}) = c + m(d/(\phi\lambda))$$
$$Kn = c \cdot \mathrm{E} \cdot e^{m\frac{d}{\phi\lambda}} \tag{17}$$

where E is the elastic modulus (Pa), c is the intercept of the linearized relation and m is its slope (Figure 13b).

4.2. Linking Permeability and Stiffness

With specific stiffness linked to key mechanical and morphological properties of the fracture, the permeability may also be linked. We rearrange Equation 17 in terms of fracture closure, d, to recover:

$$d = \frac{\phi\lambda \ln\left(\frac{Kn}{\mathrm{E}}\right) - c}{m} \tag{18}$$

combining the relationship between aperture, b, and closure, d, as noted in Table 1, and the validated cubic law in Figure 10, permeability change may be rewritten as:

$$\frac{k}{k_0} = \left(1 + \frac{-d}{b_0}\right)^3 \tag{19}$$

Then substituting Equation 18 into Equation 19 yields:

$$\frac{k}{k_0} = \left(1 + \frac{c - \ln\left(\frac{Kn}{E}\right)\phi\lambda}{mb_0}\right)^3 \tag{20}$$

Thus, we obtain a dimensionless relationship that links permeability to specific stiffness as a function of modulus and characteristics of the rough surface, inclusive of shear offset. We apply this to the observed relationship between specific stiffness and permeability changes (Figure 12) to check its fidelity. The resulting relation captures the essential characteristics of interaction (Figure S5 in Supporting Information S1). Excluded from this evaluation is the region of asymptoting permeability at low porosities or high specific stiffnesses—where the permeability relation may be invalid in not accommodating disconnected porosity (Zimmerman et al., 1992). When relating the roughness of the fracture to the fitting parameters, it becomes evident that increasing roughness causes both the intercept and slope of the linear relationship to decrease. This suggests that these two parameters could serve as indicators of fracture weakening due to increased roughness for certain surfaces, providing a potential metric for assessing the mechanical impact of surface irregularities on fracture behavior. We further tested the universal applicability of Equation 20 by rescaling both stiffness and permeability (Figure S6 in Supporting Information S1) by incorporating the parameters from multiple roughness levels:

$$\left(\frac{k}{k_0}\right)^{\log_{b_0} b_0^*} = \left(1 + \frac{c - \ln\left(\frac{K\mathrm{n}}{K\mathrm{n}_0}\frac{1}{E}\right)\phi\lambda}{mb_0}\right)^3 \tag{21}$$

where b_0^* is the initial aperture of the least rough surface investigated, and $K\mathrm{n}_0$ is the fracture specific stiffness under seating pressure.

The results (Figure 14c) successfully collapse the original observations (Figure S6), like other approaches, for example, (Petrovitch et al., 2013; Pyrak-Nolte & Nolte, 2016; L. Wang & Cardenas, 2016). By comparing our rescaled data with published flow–stiffness relationship data from Pyrak-Nolte (Pyrak-Nolte & Nolte, 2016) (Figure 14a), we demonstrate consistency, particularly in the range 0.01–0.9 of the dimensionless permeability variable. Compared to their model, the initial flat effective medium regime in their data appears more pronounced, due to the use of a linear scale for Kn. Minor discrepancies are also apparent in other rescaling approaches from the previously noted studies (L. Wang & Cardenas, 2016), suggesting that while different rescaling methods

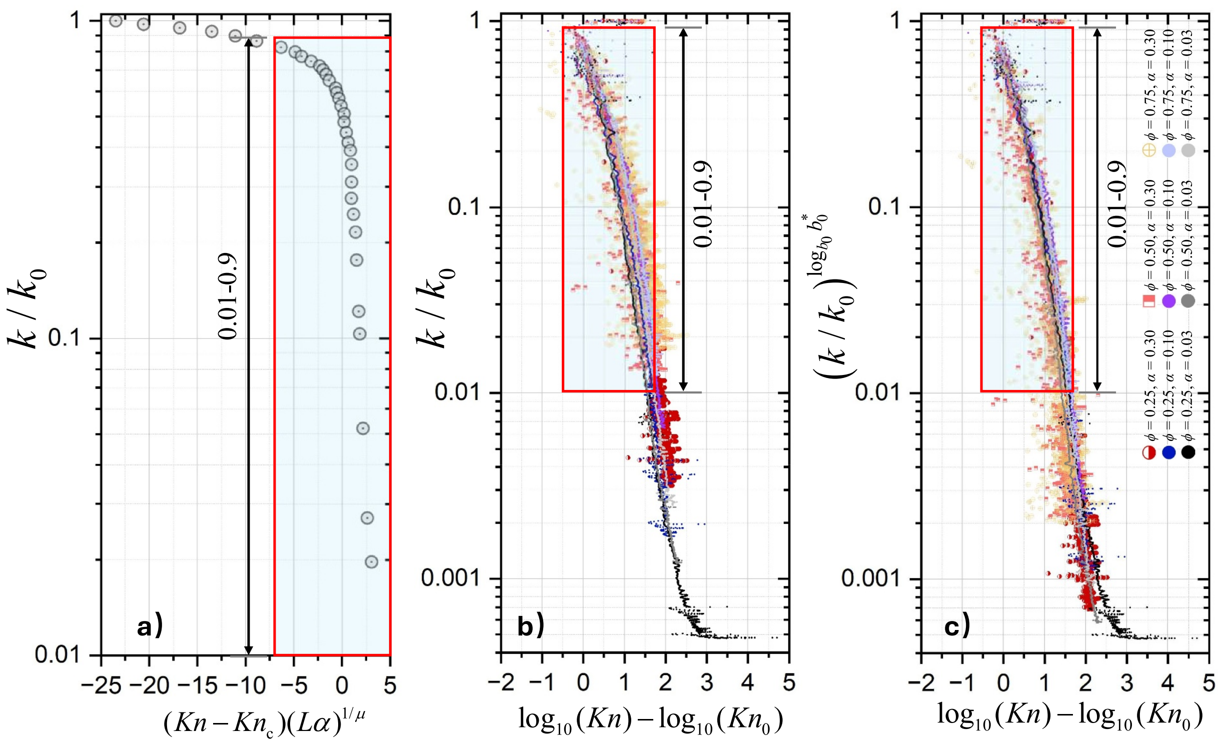

Figure 14. Rescaled relationship between permeability and specific stiffness: (a) Approach from Pyrak-Nolte (Pyrak-Nolte & Nolte, 2016) (data sampled and modified from flow to permeability); (b) Semi-rescaled permeability stiffness relationship; (c) Fully rescaled permeability stiffness relationship.

effectively collapse data across varying roughness and offset conditions, the choice of scaling approach, surface statistics controlling parameters and even stress ranges influence the shape and extent of the curves.

Overall, the predictive capability of the dimensionless relationship (Equation 21) is valuable for understanding hydro-mechanical coupling in fractured systems, as it establishes a direct connection between mechanical properties (specific stiffness) and hydraulic behavior (permeability). The ability to rescale data across varying roughness and shear offsets reinforces the universality of this approach, demonstrating that permeability evolution can be effectively captured within a unified framework. By incorporating surface roughness effects and crack influence into the formulation of the method, this approach further refines the connection between fracture structure and fluid flow dynamics, offering a relatively reliable means to estimate permeability variations from stiffness measurements. Given the observed agreement with previous scaling models, this approach holds potential for recovering permeability information from indirect geophysical measurements, such as acoustic or ultrasonic monitoring techniques, offering more pathways toward improved remote sensing and prediction of fluid flow in fractured media.

5. Conclusion

We investigate the nonlinear mechanical and hydraulic response of fractures in rock under increasing stresses. A series of DEM simulations quantify the effects of surface roughness and shear displacement offset on these properties. A universal dimensionless relationship links specific stiffness and permeability evolution, incorporating geometric controls and mechanical deformation. The main conclusions of this study are:

1. Initial porosity increases with increasing initial shear offset but ultimate porosities in the stressed fractures converge to very low magnitudes.
2. Increasing surface roughness reduces specific stiffness, with rougher surfaces and larger shear offsets further decreasing fracture stiffness. Superimposed on this trend is the cracking effect, where localized asperity rupture alters contact area and permeability evolution. The ability to explicitly capture bond breakage highlights the value of the DEM approach in modeling nonlinear fracture behavior.

3. A linear relationship between specific stiffness and normalized geometry is identified, with joint closure normalized by offset and correlation wavelength, and specific stiffness normalized by elastic modulus. This normalization codifies the relationship across a broad range of conditions, enabling a clearer understanding of how geometric characteristics influence fracture stiffness.
4. Extending from the linear stiffness-geometry relationship, specific stiffness correlates with permeability evolution, accounting for roughness and shear offset. This predictive model successfully forecasts hydro-mechanical response and suggests the feasibility of imaging permeability from active acoustic data. However, at very low porosities, permeability is overpredicted due to the model's limitation in fully capturing disconnected porosity effects.

Data Availability Statement

This study was conducted using PFC^{3D} (Particle Flow Code 3D), version 5.0, developed by Itasca Consulting Group. PFC^{3D} is a commercial discrete element modeling software. While the software is not open-source, it is publicly accessible for purchase or through institutional licenses. All relevant input data, parameters, and model configuration files used in the simulations are available at (He, 2025).

Acknowledgments
This work is a partial result of support from the US Department of Energy under grant DE-EE0007080 through Utah FORGE. We thank KJ Im for access to his flow code. DE gratefully acknowledges support from the G. Albert Shoemaker endowment. These sources of support are gratefully acknowledged.

References

Antony, S. J., Olugbenga, A., & Ozerkan, N. G. (2018). Sensing, measuring and modelling the mechanical properties of sandstone. *Rock Mechanics and Rock Engineering*, *51*(2), 451–464. https://doi.org/10.1007/s00603-017-1347-3
Archard, J. F. (1957). Elastic deformation and the laws of friction. *Proceedings of the Royal Society of London. Series A, Mathematical and Physical Sciences*.
Bandis, S. C., Lumsden, A. C., & Barton, N. R. (1983). Fundamentals of rock joint deformation. *International Journal of Rock Mechanics and Mining Sciences & Geomechanics Abstracts*, *20*(6), 249–268. https://doi.org/10.1016/0148-9062(83)90595-8
Bowden, F. P., & Tabor, D. (1950). *The friction and lubrication of solids*. Clarendon Press.
Brown, S., Caprihan, A., & Hardy, R. (1998). Experimental observation of fluid flow channels in a single fracture. *Journal of Geophysical Research*, *103*(B3), 5125–5132. https://doi.org/10.1029/97JB03542
Byerlee, J. (1978). Friction of rocks. *Rock Friction and Earthquake Prediction*, 615–626. https://doi.org/10.1007/978-3-0348-7182-2_4
Candela, T., Renard, F., Klinger, Y., Mair, K., Schmittbuhl, J., & Brodsky, E. E. (2012). Roughness of fault surfaces over nine decades of length scales. *Journal of Geophysical Research*, *117*(B8), 2011JB009041. https://doi.org/10.1029/2011JB009041
Charles, A. C. (2018). Experimental study of electrical resistivity to rock fracture intensity and aperture size. *International Journal of Physics*, *6*.
Choi, M.-K., Bobet, A., & Pyrak-Nolte, L. J. (2014). The effect of surface roughness and mixed-mode loading on the stiffness ratio κx/κz for fractures. *Geophysics*, *79*(5), D319–D331. https://doi.org/10.1190/geo2013-0438.1
Cook, N. G. W. (1992). Natural joints in rock: Mechanical, hydraulic and seismic behaviour and properties under normal stress. *International Journal of Rock Mechanics and Mining Sciences & Geomechanics Abstracts*, *29*(3), 198–223. https://doi.org/10.1016/0148-9062(92)93656-5
Cundall, P. A., & Strack, O. D. L. (1979). A discrete numerical model for granular assemblies. *Géotechnique*, *29*(1), 47–65. https://doi.org/10.1680/geot.1979.29.1.47
Dyke, C. G., & Dobereiner, L. (1991). Evaluating the strength and deformability of sandstones. *International Journal of Rock Mechanics and Mining Sciences & Geomechanics Abstracts*, *28*(6), A338. https://doi.org/10.1016/0148-9062(91)91187-v
Elsworth, D. (1984). *Laminar and turbulent flow in rock fissures and fissure networks*. University o f California.
Elsworth, D., & Mao, B. (1992). Flow-deformation response of dual-porosity media. *Journal of Geotechnical Engineering*, *118*(1), 107–124. https://doi.org/10.1061/(asce)0733-9410(1992)118:1(107)
Elsworth, D., Spiers, C. J., & Niemeijer, A. R. (2016). Understanding induced seismicity. *Science*, *354*(6318), 1380–1381. https://doi.org/10.1126/science.aal2584
Gangi, A. F. (1978). Variation of whole and fractured porous rock permeability with confining pressure. *International Journal of Rock Mechanics and Mining Sciences*, *15*(5), 249–257. https://doi.org/10.1016/0148-9062(78)90957-9
Goodman, R. E. (1975). *Methods of geological engineering in discontinuous rocks*. West Group.
Goodman, R. E., Taylor, R. L., & Brekke, T. L. (1968). A model for the mechanics of jointed rock. *Journal of the Soil Mechanics and Foundations Division*, *94*(3), 637–659. https://doi.org/10.1061/JSFEAQ.0001133
Gottsmann, J., Neuberg, J., & Scheu, B. (Eds.) (2019)., *Volcanic unrest: From science to society*. Springer International Publishing. https://doi.org/10.1007/978-3-319-58412-6
Greenwood, J. A. (1967). The area of contact between rough surfaces and flats. *Journal of Tribology*, *89*(1), 81–87. https://doi.org/10.1115/1.3616906
Guglielmi, Y., Cappa, F., Avouac, J.-P., Henry, P., & Elsworth, D. (2015). Seismicity triggered by fluid injection–induced aseismic slip. *Science*, *348*(6240), 1224–1226. https://doi.org/10.1126/science.aab0476
Hadjigeorgiou, J., Esmaieli, K., & Grenon, M. (2009). Stability analysis of vertical excavations in hard rock by integrating a fracture system into a PFC model. *Tunnelling and Underground Space Technology*, *24*(3), 296–308. https://doi.org/10.1016/j.tust.2008.10.002
He, X. (2025). Xinxin-He/Fractured-Rock-Samples: v1.0 (Version 1.0) [Dataset]. *Zenodo*. https://doi.org/10.5281/zenodo.15014849
Hopkins, D. L. (1991). *The effect of surface roughness on joint stiffness, aperture, and acoustic wave propagation*. (Doctor). University of California.
Im, K., Elsworth, D., & Wang, C. (2019). Cyclic permeability evolution during repose then reactivation of fractures and faults. *Journal of Geophysical Research: Solid Earth*, *124*(5), 4492–4506. https://doi.org/10.1029/2019JB017309
Leopold Müller, S. (1963). *Der Felsbau, Band 1, Theoretischer Teil*. Springer Spektrum. https://doi.org/10.1007/978-3-662-58196-4
Lubbe, R., Sothcott, J., Worthington, M. H., & McCann, C. (2008). Laboratory estimates of normal and shear fracture compliance. *Geophysical Prospecting*, *56*(2), 239–247. https://doi.org/10.1111/j.1365-2478.2007.00688.x

Luo, S., Zhao, Z., Peng, H., & Pu, H. (2016). The role of fracture surface roughness in macroscopic fluid flow and heat transfer in fractured rocks. *International Journal of Rock Mechanics and Mining Sciences*, *87*, 29–38. https://doi.org/10.1016/j.ijrmms.2016.05.006

Manga, M., Beresnev, I., Brodsky, E. E., Elkhoury, J. E., Elsworth, D., Ingebritsen, S. E., et al. (2012). Changes in permeability caused by transient stresses: Field observations, experiments, and mechanisms. *Reviews of Geophysics*, *50*(2). https://doi.org/10.1029/2011RG000382

Martínez, Á. R., Roubinet, D., & Tartakovsky, D. M. (2014). Analytical models of heat conduction in fractured rocks. *Journal of Geophysical Research: Solid Earth*, *119*(1), 83–98. https://doi.org/10.1002/2012JB010016

McCool, J. I. (1986). Comparison of models for the contact of rough surfaces. *Wear*, *107*(1), 37–60. https://doi.org/10.1016/0043-1648(86)90045-1

Méheust, Y., & Schmittbuhl, J. (2000). Flow enhancement of a rough fracture. *Geophysical Research Letters*, *27*(18), 2989–2992. https://doi.org/10.1029/1999GL008464

Myer, L. R., Pyrak-Nolte, L. J., & Cook, N. G. W. (1990). Effects of single fractures on seismic wave propagation.

Nakagawa, S., Nihei, K. T., & Myer, L. R. (2004). Plane wave solution for elastic wave scattering by a heterogeneous fracture. *Journal of the Acoustical Society of America*, *115*(6), 2761–2772. https://doi.org/10.1121/1.1739483

Nakagawa, S., Nihei, K. T., Myer, L. R., & Majer, E. L. (2003). Three-dimensional elastic wave scattering by a layer containing vertical periodic fractures. *Journal of the Acoustical Society of America*, *113*(6), 3012–3023. https://doi.org/10.1121/1.1572139

Petrovitch, C. L., Nolte, D. D., & Pyrak-Nolte, L. J. (2013). Scaling of fluid flow versus fracture stiffness. *Geophysical Research Letters*, *40*(10), 2076–2080. https://doi.org/10.1002/grl.50479

Petrovitch, C. L., Pyrak-Nolte, L. J., & Nolte, D. D. (2014). Combined scaling of fluid flow and seismic stiffness in single fractures. *Rock Mechanics and Rock Engineering*, *47*(5), 1613–1623. https://doi.org/10.1007/s00603-014-0591-z

Potyondy, D. O., & Cundall, P. A. (2004). A bonded-particle model for rock. *International Journal of Rock Mechanics and Mining Sciences*, *41*(8), 1329–1364. https://doi.org/10.1016/j.ijrmms.2004.09.011

Pyrak-Nolte. (2019). Fracture specific stiffness. In *Science of carbon storage in deep saline formations* (pp. 311–335). Elsevier. https://doi.org/10.1016/B978-0-12-812752-0.00014-9

Pyrak-Nolte, L. J., & Morris, J. P. (2000). Single fractures under normal stress: The relation between fracture specific stiffness and fluid flow. *International Journal of Rock Mechanics and Mining Sciences*, *37*(1–2), 245–262. https://doi.org/10.1016/s1365-1609(99)00104-5

Pyrak-Nolte, L. J., Myer, L. R., & Cook, N. G. W. (1990a). Anisotropy in seismic velocities and amplitudes from multiple parallel fractures. *Journal of Geophysical Research*, *95*(B7), 11345–11358. https://doi.org/10.1029/JB095iB07p11345

Pyrak-Nolte, L. J., Myer, L. R., & Cook, N. G. W. (1990b). Transmission of seismic waves across single natural fractures. *Journal of Geophysical Research*, *95*(B6), 8617–8638. https://doi.org/10.1029/JB095iB06p08617

Pyrak-Nolte, L. J., & Nolte, D. D. (1992). Frequency dependence of fracture stiffness. *Geophysical Research Letters*, *19*(3), 325–328. https://doi.org/10.1029/91GL03179

Pyrak-Nolte, L. J., & Nolte, D. D. (2016). Approaching a universal scaling relationship between fracture stiffness and fluid flow. *Nature Communications*, *7*(1), 10663. https://doi.org/10.1038/ncomms10663

Sawayama, K., Ishibashi, T., Jiang, F., & Tsuji, T. (2023). Relationship between permeability and resistivity of sheared rock fractures: The role of tortuosity and flow path percolation. *Geophysical Research Letters*, *50*(20), e2023GL104418. https://doi.org/10.1029/2023GL104418

Shokouhi, P., Jin, J., Wood, C., Rivière, J., Madara, B., Elsworth, D., & Marone, C. (2020). Dynamic stressing of naturally fractured rocks: On the relation between transient changes in permeability and elastic wave velocity. *Geophysical Research Letters*, *47*(1), e2019GL083557. https://doi.org/10.1029/2019GL083557

Swan, G. (1983). Determination of stiffness and other joint properties from roughness measurements. *Rock Mechanics and Rock Engineering*, *16*(1), 19–38. https://doi.org/10.1007/BF01030216

Talobre, A. (1957). *La mécanique des roches: appliqueé aux travaux publics*. Dunod.

Wang, C., Elsworth, D., Fang, Y., & Zhang, F. (2020). Influence of fracture roughness on shear strength, slip stability and permeability: A mechanistic analysis by three-dimensional digital rock modeling. *Journal of Rock Mechanics and Geotechnical Engineering*, *12*(4), 720–731. https://doi.org/10.1016/j.jrmge.2019.12.010

Wang, K., Zhang, G., Wang, Y., Zhang, X., Li, K., Guo, W., & Du, F. (2022). A numerical investigation of hydraulic fracturing on coal seam permeability based on PFC-COMSOL coupling method. *International Journal of Coal Science & Technology*, *9*(1), 10. https://doi.org/10.1007/s40789-022-00484-2

Wang, L., & Cardenas, M. B. (2016). Development of an empirical model relating permeability and specific stiffness for rough fractures from numerical deformation experiments. *Journal of Geophysical Research: Solid Earth*, *121*(7), 4977–4989. https://doi.org/10.1002/2016JB013004

Wang, T., Elsworth, D., He, Y., Zhao, X., Wang, S., Xu, D., & Lei, M. (2023). Impact of loading rate on the mechanical behavior of jointed rock. *Geomechanics and Geophysics for Geo-Energy and Geo-Resources*, *9*(1), 127. https://doi.org/10.1007/s40948-023-00669-2

Wang, Y., Han, D.-H., Li, H., Zhao, L., Ren, J., & Zhang, Y. (2020). A comparative study of the stress-dependence of dynamic and static moduli for sandstones. *Geophysics*, *85*(4), MR179–MR190. https://doi.org/10.1190/geo2019-0335.1

Whitehouse, D. J., & Archard, J. F. (1970). The properties of random surfaces of significance in their contact. *Proceedings of the Royal Society of London. A. Mathematical and Physical Sciences*, *316*(1524), 97–121. https://doi.org/10.1098/rspa.1970.0068

Witherspoon, P. A., Wang, J. S. Y., Iwai, K., & Gale, J. E. (1980). Validity of Cubic Law for fluid flow in a deformable rock fracture. *Water Resources Research*, *16*(6), 1016–1024. https://doi.org/10.1029/WR016i006p01016

Wood, C. E., Manogharan, P., Rathbun, A., Rivière, J., Elsworth, D., Marone, C., & Shokouhi, P. (2024). Relating hydro-mechanical and elastodynamic properties of dynamically stressed tensile-fractured rock in relation to applied normal stress, fracture aperture, and contact area. *Journal of Geophysical Research: Solid Earth*, *129*(8), e2023JB027676. https://doi.org/10.1029/2023JB027676

Worthington, M. (2007). The compliance of macrofractures. *The Leading Edge*, *26*(9), 1118–1122. https://doi.org/10.1190/1.2780780

Worthington, M. (2008). Interpreting seismic anisotropy in fractured reservoirs. *First Break*, *26*(7). https://doi.org/10.3997/1365-2397.2008008

Yang, W., Geng, Y., Zhou, Z., Li, L., Gao, C., Wang, M., & Zhang, D. (2020). DEM numerical simulation study on fracture propagation of synchronous fracturing in a double fracture rock mass. *Geomechanics and Geophysics for Geo-Energy and Geo-Resources*, *6*(2), 39. https://doi.org/10.1007/s40948-020-00162-0

Yasuhara, H., Elsworth, D., & Polak, A. (2004). Evolution of permeability in a natural fracture: Significant role of pressure solution. *Journal of Geophysical Research*, *109*(B3), 2003JB002663. https://doi.org/10.1029/2003JB002663

Yin, H., Zhao, J., Tang, G., Zhao, L., Ma, X., & Wang, S. (2017). Pressure and fluid effect on frequency-dependent elastic moduli in fully saturated tight sandstone. *Journal of Geophysical Research: Solid Earth*, *122*(11), 8925–8942. https://doi.org/10.1002/2017JB014244

Yoon, J. (2007). Application of experimental design and optimization to PFC model calibration in uniaxial compression simulation. *International Journal of Rock Mechanics and Mining Sciences*, *44*(6), 871–889. https://doi.org/10.1016/j.ijrmms.2007.01.004

Zhao, W., Huang, R., & Yan, M. (2015). Mechanical and fracture behavior of rock mass with parallel concentrated joints with different dip angle and number based on PFC simulation. *Geomechanics and Engineering*, *8*(6), 757–767. https://doi.org/10.12989/GAE.2015.8.6.757

Zheng, B., & Elsworth, D. (2012). Evolution of permeability in heterogeneous granular aggregates during chemical compaction: Granular mechanics models. *Journal of Geophysical Research*, *117*(B3), 2011JB008573. https://doi.org/10.1029/2011JB008573

Zheng, B., & Elsworth, D. (2013). Strength evolution in heterogeneous granular aggregates during chemo–mechanical compaction. *International Journal of Rock Mechanics and Mining Sciences*, *60*, 217–226. https://doi.org/10.1016/j.ijrmms.2012.12.031

Zimmerman, R. W., & Bodvarsson, G. S. (1996). Hydraulic conductivity of rock fractures. *Transport in Porous Media*, *23*(1). https://doi.org/10.1007/BF00145263

Zimmerman, R. W., Chen, D.-W., & Cook, N. G. W. (1992). The effect of contact area on the permeability of fractures. *Journal of Hydrology*, *139*(1–4), 79–96. https://doi.org/10.1016/0022-1694(92)90196-3

Zimmerman, R. W., & Yeo, I.-W. (2000). Fluid flow in rock fractures: From the Navier-Stokes equations to the cubic law. In B. Faybishenko, P. A. Witherspoon, & S. M. Benson (Eds.), *Geophysical monograph series* (Vol. 122, pp. 213–224). American Geophysical Union. https://doi.org/10.1029/GM122p0213